JOURNAL OF GEOPHYSICAL RESEARCH, VOL. ???, XXXX, DOI:10.1002/,

MLT dependence in the relationship between plasmapause, solar wind and geomagnetic activity based on CRRES: 1990-1991

Mario Bandić,[1] Giuli Verbanac,[2] Mark B. Moldwin,[3] Viviane Pierrard[4], and Giovanni Piredda[5]

Corresponding author: G. Verbanac, (giuli1.verbanac@gmail.com)

[1]Preziosastr. 15a, 81927 München, Germany

[2]Department of Geophysics, University of Zagreb, Croatia

[3]Climate and Space Sciences and Engineering, University of Michigan, USA.

[4]Royal Belgian Institute for Space Aeronomy (Space Physics and STCE), Brussels, Belgium

[5]University of Applied Sciences, Dornbirn, Austria

Key Points.

- The delay times of Lpp to the arrival of Lpp indicators is a function of MLT
- The MLT dependence of plasmapause formation is in agreement with the mechanism of interchange instability
- At high geomagnetic activity the Lpp bulge is formed in the postdusk. At low geomagnetic activity the bulge is located close to midnight

Abstract. Using the database of CRRES in situ observations of the plasmapause crossings, we develop linear and more complex plasmapause models parametrized by (a) solar wind parameters V (solar wind velocity), BV (where B is the magnitude of the interplanetary magnetic field IMF), and $d\Phi_{mp}/dt$ (which combines different physical mechanisms which run magnetospheric activity), and (b) geomagnetic indices Dst, Ap and AE. The complex models are built by including a first harmonic in MLT. Our method based on the cross correlation analyses provides not only the plasmapause shape for different levels of geomagnetic activity, but additionally yields the information of the delays in the MLT response of the plasmapause. All models based on both solar wind parameters and geomagnetic indices indicate the maximal plasmapause extension in the postdusk side at high geomagnetic activity. The decrease in the convection electric field places the bulge toward midnight. These results are compared and discussed in regards to past works. Our study shows that the time delays in the plasmapause response are function of MLT and suggests that the plasmapause is formed by the mechanism of interchange instability motion. We observed that any change quickly propagates across

dawn to noon, and then at lower rate toward midnight. The results further indicate that the instability may propagate much faster during solar maximum than around solar minimum.

This study contributes to the determination of the MLT dependence of the plasmapause and to constrain physical mechanism by which the plasmapause is formed.

1. Introduction

The plasmasphere is an area in the inner magnetosphere which contains trapped, low-energy, and dense plasma. The plasmapause is the outer boundary of the plasmasphere whose dynamics are determined by a combination of the two electric fields: corotation and convection electric fields [e.g., *Nishida*, 1966; *Lemaire and Gringauz*, 1998].

Since plasmapause influences the ring current dynamic [e.g., *Kozyra et al.*, 1995], radiation belts [e.g., *Horne and Thorne*, 1998; *Lorentzen et al.*, 2001; *Darrouzet et al.*, 2013], formation and propagation of electromagnetic waves [e.g., *Takahashi and Anderson*, 1992] it is important to know its time dependent location.

The plasmapause positions (L_{PP}) have been estimated both theoretically and empirically. The L_{PP} dynamics are studied theoretically by considering (i) the last closed equipotential of the convection electric field [*Brice*, 1967; *Lemaire and Pierrard*, 2008], (ii) the peeling of the plasmasphere [*Lemaire and Gringauz*, 1998; *Pierrard and Lemaire*, 2004; *Lemaire and Pierrard*, 2008]. This second process implicates a MLT dependence of the plasmapause position that can be verified empirically. Empirically L_{PP} has been evaluated by studying: ground based whistler data; in situ satellite observations of plasma density (e.g., ISEE, CRRES), electron plasma frequency (CLUSTER), and thermal velocity (THEMIS); field aligned current observations (CHAMP), as a function of geomagnetic indices [e.g., *O'Brien and Moldwin*, 2003; *Liu et al.*, 2015; *Verbanac et al.*, 2015, and reference therein] and solar wind parameters [*Larsen et al.*, 2007; *Cho et al.*, 2015; *Verbanac et al.*, 2015]. All these studies have shown that the plasmapause shrinks when geomagnetic activity increases achieving the largest extension in the dusk side.

Most of the previous empirical studies used the maximum (or minimum) in the geomagnetic indices or in the solar wind (thereafter SW) parameters during hours to days prior to the plasmapause crossing. For instance, *Carpenter and Anderson* [1992] established linear relationship between L_{PP} and the maximum of geomagnetic Kp index observed in the previous 24 hours relative to the plasmapause crossing. *Moldwin et al.* [2002] linked the L_{PP} with the maximum Kp index found in the previous 12 hours separately for night, dawn, day and dusk sectors. *O'Brien and Moldwin* [2003] obtained linear relationships between L_{PP} and maximum Kp index taken from 36 to 2 hours relative to the plasmapause crossing, maximum AE index and minimum Dst index taken in the previous 36 hours and 24 hours, respectively. They also fitted a function to the observed L_{PP} values that depends both on geomagnetic indices and MLT. Following this work, *Liu and Liu* [2014] obtained plasmapause model based on THEMIS measurements. Similarly, *Heilig and Lühr* [2013] expressed L_{PP} based on field-aligned currents as a function of Kp, Kp^2 and MLT. *Cho et al.* [2015] presented the models averaged in MLTs, based on THEMIS plasmapause crossings and extrema (minimum or maximum) of some solar wind variables (e.g., velocity V, z-component of the IMF vector B_z, Akasofu's epsilon parameter, y component of the solar wind electric field E, IMF clock angle θ) and geomagnetic indices Kp, Dst and AE, all taken within the selected time windows. *Liu et al.* [2015] obtained multi-index plasmapause model also using THEMIS measurements and geomagnetic indices: mean AE, mean Kp, mean AL, maximum AU and maximum SYM_H taken within the determined time window for each input parameter and for each MLT sector.

Larsen et al. [2007] provide the delay in the response of plasmapause averaged in MLT to the arrival of B_z, θ and polar cap potential drop ϕ. *Verbanac et al.* [2015] obtained

L_{PP} fits for three different MLT sectors (night, day, evening) based on solar wind coupling functions (B_z, BV and $d\Phi_{mp}/dt$ defined in section 2) and geomagnetic indices (Ap, Dst and AE). They showed that different regions of the plasmapause react with different delay times to the arrival of the investigated L_{PP} indicators which are function of MLT.

In the present study, we apply the approach presented in *Verbanac et al.* [2015] (hereafter Paper I) to the CRESS based L_{PP} database developed by *Moldwin et al.* [2002] (hereafter Paper II) that contains about three time more data than analysed in Paper I and during a more geomagnetically active period.

Worth noting is that the MLT dependence of the time lags in the response of plasmapause obtained with our method is very valuable information which can help in constraining the physical mechanism by which the plasmapause is formed.

The mains aims are:

(i) to investigate the MLT dependence in the relationship between CRRES-based plasmapause, solar wind and geomagnetic activity;

(ii) to compare the obtained plasmapause shapes with those derived from different models;

(iii) to investigate the response of the plasmapause to L_{PP} indicators during different phases of the solar activity cycle;

(iv) try to constrain physical mechanism by which the plasmapause is formed.

We build simple empirical L_{PP} models using solar wind parameters V, BV, $d\Phi_{mp}/dt$ and geomagnetic indices Ap, Dst, AE as indicators of the L_{PP} for different MLT sector divisions and investigate the dependence of the obtained delay times on MLTs. We further develop more complex models by including a first harmonic in MLT. The results are compared with those obtained by other studies in order to discuss the plasmapause shape from different models. Further comparison of the obtained time delays with those based on Cluster plasmapause as presented in Paper I is performed to investigate the plasmapause responses during different phases of solar activity cycle.

The paper is organized as follows. Data and method of analyses are presented in section 2. section 3 contains the results of the obtained best linear fits and of the continuous MLT models. Comparison with results from other studies is given in section 4. Discussion is given in section 5 and conclusions are drawn in the last section.

2. Data and Method

To study the L_{PP} we used following data:

- one-hour averages of geomagnetic indices Dst and AE;
- three-hour averages of the geomagnetic index Ap;
- one-hour averages of the solar wind velocity V, IMF magnitude B and components B_x, B_y, B_z in GSM (Geocentric Solar Magnetospheric) of the IMF vector $\mathbf{B}$;
- dataset of plasmapause positions based on the plasma wave receiver that was onboard CRRES satellite.

Within the studied period there are a lot of gaps in the solar wind data, which are often long lasting (5-8 days). Roughly 55% of solar wind data is missing.

We used the dataset of 963 plasmapause positions obtained from in situ CRRES electron density observations made in 1990-1991. For the description of the methodology employed to identify the L_{PP} we refer to Paper II. There is a gap in the data coverage around noon at larger radial distances and near midnight at middle radial distance. Also, because of the orbital characteristics plasmapause at L shell >7 could not be collected.

We employed the following solar wind based L_{PP} indicators: V, BV and $d\Phi_{mp}/dt$ [*Newell et al.*, 2007] defined as:

$$\Phi_{mp}/dt = V^{4/3} B_T^{2/3} sin^{8/3}(\theta_c/2) \quad (1)$$

where $B_T = \sqrt{B_y^2 + B_z^2}$ and $\theta_c = \arctan(B_y/B_z)$.

For these solar wind parameters we were able to obtain stable cross-correlation results. The importance of solar wind coupling functions BV and $d\Phi_{mp}/dt$ in accounting for much about the magnetospheric activity is explained in our previous work (Paper I). Here we only shortly discuss their physical meaning. B_z is related to the reconnection of the IMF with the Earth's magnetic field, the process that is important for strengthening the magnetospheric convection. BV is proportional to the interplanetary electric field. $d\Phi_{mp}/dt$ takes into account different physical processes related to the magnetospheric activity. In addition to the previously mentioned solar wind parameters, past work has shown that the plasmapause location is well correlated with V [*Cho et al.*, 2015]. Furthermore, *Verbanac et al.* [2011, 2013] have reported a strong relationship between geomagnetic indices and V during both solar minimum and solar maximum. We therefore also test the plasmapause response to this solar wind parameter in this study.

The relationships between the L_{PP} and L_{PP} indicators are investigated binning the data in three and four MLT sectors as follow:

- three sectors: Sector1-night (01-07 MLT), Sector2-day (07-16 MLT), Sector3-evening (16-01 MLT);

- four "traditional" sectors: SectorI (00-06 MLT), SectorII (06-12 MLT), SectorIII (12-18 MLT), SectorIV (18-00 MLT);

and also when all MLTs are taken together.

The MLT intervals in both three and four sector divisions were carefully chosen to provide reliable statistics in each time bin. The three sector division is the same as in Paper I, allowing us to directly compare the obtained results with our previous work.

Employing the cross-correlation analysis we obtain the time lags of the plasmapause response to L_{PP} indicators and linear least-squares fit parameters for the highest correlation time lags which describe the relationship between the L_{PP} and different L_{PP} indicators. Following our previous study (Paper I) we consider here the time window of 30 hours before the plasmapause crossings. For detailed description of the employed cross-correlation analysis, the reader is referred to Paper I.

Concerning solar wind based L_{PP} indicators, the cross-correlation analyses are performed only if there were $\geq 70\%$ data in the interval of 30 hours preceding the UT of each of the plasmapause crossing. Imposing this criterion, we analyse $\sim$300 L_{PP}, similar to the number of L_{PP} investigated in PaperI, which is adequate to perform reliable statistics. The number of plasmapause positions meeting this condition for each of the solar wind L_{pp} indicator in both three and four sector divisions is given in Table 1. For geomagnetic indices (thereafter GI), all the available L_{pp} in each sector are used (in total 963 L_{pp}), and the numbers are also displayed in Table 1. Note that in four sector division, SectorIII (12-18 MLT) contains significantly less data than other sectors. For solar wind based L_{PP} indicators, the numbers of L_{pp} are additionally reduced due to the gaps in solar wind data. Thus for solar wind parameters we focus on the three sector division only in order to ensure reliable statistics.

3. Results

3.1. Best linear fit models

Here we present the results obtained employing the cross-correlation analysis, as explained in the previous section. In Table 2 we present the time lags Δt, and the RMS errors (RMSE) of the best fits obtained by binning the data into three MLT sectors (01-07 MLT, 07-16 MLT, 16-01 MLT) as well as for all MLTs taken together. The correlation coefficients are given for the case when all MLTs are taken together. For GI we additionally show Δt and RMSE of the best fits for four MLT sector divisions (00-06 MLT, 06-12 MLT, 12-18 MLT, 18-00 MLT) in Table 3.

The RMS errors displayed in both tables are approximately 0.6-1 L in all MLTs taken together or in sectors. The sectors that comprise dusk and evening (Sector3 in the three sector division and SectorIV in the four sector division) have considerably more scatter than the other MLT sectors. The lowest model RMSEs found in Sector2 for three sector division and in SectorIII for four sector division likely reflect the absence of $L_{PP} > 5$ on the dayside and generally less plasmapause data between 12 MLT and 18 MLT (for the details about the data coverage the reader is referred to Paper II). We calculate the statistical significance of the RMSE differences between models using a Monte Carlo bootstrap procedure. We first generate distributions of RMSEs for each model by creating the data samples from the original data set using random selection with replacement. For each pair of the RMSE distributions within each column of Table 2 and Table 3 we then calculate the probability to observe a larger RMSE in the first distribution belonging to the pair than in the second. If this probability is larger than 0.95 or smaller than 0.05 then the two RMSEs are considered to be distinguishable. These calculations provide following results. For three sectors division, only Dst in the day sector (07-16 MLT) provides a relatively superior model since it is the only model which is statistically distinguishable from Ap model even if not from all other L_{PP} models. The RMSEs of all other models are not statistically distinguishable from the RMSEs of any model. Note that although V in Sector2 (07-16 MLT) has the same RMSE as Dst, and lower than other L_{PP} indicators, the probability of observing larger RMSE than any of the others, taken individually, is of the order of 10%. For four sector division Dst is statistically distinguishable from both Ap and AE in SectorII (06-12 MLT), and provide the best model in this sector. Note that AE in SectorIII (12-18 MLT) has the lowest RMSE, but there is no statistical significance of the differences in regards to Dst and Ap models. Our calculations give 25% percent probability of observing a higher value of AE RMSE than the RMSE observed for the other two models.

The main conclusion that comes out of Table 2 and Table 3 is that for all L_{PP} indicators, the time lag corresponding to the highest correlation is a function of MLT. The obtained time lags ascend from Sector1 to Sector3/SectorIV. The only exception is parameter V, where the lags in Sector1 and Sector2 are comparable. Similar Δts are obtained for Ap and AE, and notably shorter Δt for Dst and V (2-12 hours shorter depending on the sector). Intermediate lags are found for both BV and $d\Phi_{mp}/dt - L_{pp}$. Time lag versus MLT is shown in Figure 1. The plotted lags are obtained by binning the data into 6-hours MLT for GI, and into three MLT sectors for solar wind based L_{PP} indicators. We note here that the observed MLT dependence of the time lags indicates that the plasmapause is first formed in the postmidnight to dawn side, and later in other MLTs. The more detailed discussion is given in section 4.

The coefficients of the best linear fit models are given in Table 4. We present the fit coefficients for three sector division in order to analyse them for all L_{PP} indicators. Recall that for solar wind based L_{PP} indicators, data could not be adequately described if binned into four MLT sectors, due to the lower number of L_{PP} between 12 MLT and 18 MLT and due to additional gaps in the solar wind data.

The shape of the plasmapause was examined in respect to low and high values of L_{PP} indicators as identified from the analysed datasets. However, note that the developed models work for any given geomagnetic index or solar wind parameters, thus not only for some extreme values (low and high values). In Table 5 the fitted L_{PP} values for low and high geomagnetic activity are shown. Based on all L_{PP} relationships, the lowest L_{PP} is found in Sector2 and amounts $\sim 2.8\ R_E$. We link this L_{PP} value to the indicator values at high geomagnetic activity.

The L_{PP} values reported in Table 5 together with the RMSE given in Table 2 indicate that at quiet time the bulge is likely located in the premidnight side as concerning GI. The given solar wind based plasmapause values are indistinguishable in Sector1 and Sector3 within the error limits. At higher activity the bulge is located in Sector3 according to all L_{PP} indicators.

Figure 2 shows the location of the plasmapause for each model for two identified levels of geomagnetic activity as given in Table 5.

3.2. Continuous MLT models

We further develop more complex models by including a first harmonic in MLT.

For a certain L_{pp} indicator Q at a given MLT, plasmapause position is expressed as:

$$L_{pp} = AA \cdot Q + BB \tag{2}$$

AA and BB are defined as:

$$AA(\phi) = a_1\ [1 + a_{mlt}\ cos(\phi - a_\phi)]; \qquad BB(\phi) = b_1\ [1 + b_{mlt}\ cos(\phi - b_\phi)] \tag{3}$$

where $\phi = 2\pi(MLT/24)$.

To determine the set of model coefficients (a_1, a_{mlt}, a_ϕ, b_1, b_{mlt} and b_ϕ), firstly some finite MLT division has to be chosen. A linear regression in each sector is then performed (L_{pp}=aQ+b) and pairs of coefficients a and b are obtained, by which the model coefficients are calculated. As initial MLT bins, we selected four MLT sector division to maximize as much as possible the resolution in MLT but also to enable enough data in each sector for adequate statistics. This unfortunately allows us only to build models using geomagnetic indices. Recall that for solar wind based L_{pp} indicators, only binning the data into three MLT sectors was possible. The parameters of the obtained MLT plasmapause model are given in Table 6. The errors of the parameters are calculated with a Monte Carlo approach. We generate samples of the distribution of the linear regression coefficients (a and b) assuming that they are independent and distributed with Gaussian probability. For each sample we then calculate the model coefficients in order to obtain their probability distribution from which we determine their standard deviations. In this way we didn't have to assume that the errors are small, as required by e.g., error-propagation formulae.

The RMSE reported in Table 6 are very similar to those for simpler models given in Table 3. Only when all local times are considered, the RMSE are reduced compared to simpler models.

We note that following coefficients and their products, a_ϕ, b_ϕ, $a_1 Q + b_1$, $a_1 a_{mlt} Q$ and $b_1 b_{mlt}$, determine the plasmapause shape. The location of the bulge is given by the phase containing the combination of these coefficient products, and not with a_ϕ, b_ϕ solely as argued in *O'Brien and Moldwin* [2003].

Right panels in Figure 3 depict L_{pp}(MLT) for each model and for two levels of geomagnetic activity, as given in Table 5. Blue and red lines indicate low and high activity, respectively. The symbols show the MLT of maximum L_{pp} for each continuous model. To compare with the simpler models obtained from the cross-correlation analysis, we also show the L_{pp} in four-MLT bins (left panels). Simple Ap and Dst models for low activity cannot resolve whether the maximum plasmapause extension is in SectorI or in SectorIV, while simple AE model indicates the bulge location in SectorIV. Continuous MLT models give a maximum L_{pp} between 22 MLT and 0 MLT, depending on the model. At high activity the bulge is observed in SectorIV, according to all of simple models. Continuous models provide the maximum L_{pp} at around 21 MLT. All these indicate the midnight/premidnight plasmapause bulge which rotates toward dusk as geomagnetic activity increases.

4. Comparison with past studies

In the following we first compare the plasmapause shapes from our models (denoted as CRRES2 models) with those presented by *O'Brien and Moldwin* [2003]; *Liu and Liu* [2014]; *Liu et al.* [2015] (denoted as CRRES1, THEMIS1, and THEMIS2 models, respectively).

We could compare only our models that are based on geomagnetic indices with others, since none of these previous models are based on solar wind parameters. The past studies utilize the procedure of identifying the time window in respect to the plasmapause crossing over which the maximum (or minimum) or/and mean of the L_{pp} indicator is then determined. This approach is widely used for plasmapause modeling [e.g., *Carpenter and Anderson*, 1992; *Moldwin et al.*, 2002; *Cho et al.*, 2015]. On the other side, our method employs the L_{pp} indicator values at the highest correlation time lags and additionally provides the delays in the MLT response of the plasmapause. For comparison, plasmapause is simulated for two levels of geomagnetic activity (low and high) using each of these models. For CRRES1, THEMIS1 and CRRES2 the comparison is performed for both AE and Dst based models. When calculating predictions from CRRES1 and THEMIS1 models, the geomagnetic index values are taken as: AE=80 nT and Dst=-2 nT at low geomagnetic activity; AE=1200 nT and Dst=-250 nT at high geomagnetic activity. Plasmapause from THEMIS2 model is derived by setting the inputs at low geomagnetic activity to: mean AE=30 nT, mean Kp=1, mean AL=-20 nT, maximum AU=15 nT, maximum SYM_H=-20 nT. For high geomagnetic activity the parameters are taken as: mean AE=800 nT, mean Kp=4, mean AL=-560 nT, maximum AU=400 nT, maximum SYM_H=-260 nT. Here, it is important to note that these values used to obtain model predictions cannot be the same for our CRRES2 models because the peak values of the geomagnetic index or SW parameter are generally higher than the one obtained at the highest correlation time lag (see Table 2 and Table5 in *Verbanac et al.* [2015]). For CRRES2 we set AE=2 nT and Dst=30 nT at low geomagnetic activity; AE=700 nT and Dst=-70 nT at high geomagnetic activity. In Figure 4 plasmapause shapes obtained from CRRES1, CRRES2, THEMIS1, and THEMIS2 models are directly compared. At low geomagnetic activity, CRRES1, CRRES2, and THEMIS2 models give the bulge in the night side, from 21 MLT to 03 MLT depending on the used geomagnetic index. In contrast, the THEMIS1 models place the bulge on the day side. However, note that the plasmapause from CRRES1, CRRES2, and THEMIS1 is relatively circular with the difference between its maximum and minimum extension only about 0.5 R_E. Only CRRES1 AE based model give a bulge comparable to THEMIS2 model, with difference between the lowest and the largest L_{pp} of around 2 R_E. At higher geomagnetic activity, all models gives the bulge between 18 MLT and 21 MLT. The difference between the minimum and maximum L_{pp} extension is somewhat larger than at low activity, and is again more pronounced for THEMIS2 model (amounting for ~ 2.5 R_E) than for other three models. Generally, THEMIS2 model provides the largest plasmapause variations. This model is built by multi-index fitting using the largest number of plasmapause crossings. On the other side, CRRES1, THEMIS1 and CRRES2 models are obtained by including a first harmonic in MLT providing more smoothed plasmapause shapes. The plasmapause extension within each model (CRRES1, CRRES2, and THEMIS1) is different for AE and Dst at both levels of geomagnetic activity. In general, AE models give somewhat larger plasmapause than Dst models. We note that these differences between AE and Dst models are lower for our CRRES2 model. The RMSE values of CRRES1, CRRES2, THEMIS1, and THEMIS2 models are similar, approximately in the range 0.5-1 L. THEMIS2 has the lowest RMSE in postmidnight and dawn side (see Figure6 in *Liu et al.* [2015]). All these models have the largest RMSE in dusk side and night side.

Discontinuous models obtained from CLUSTER based plasmapause presented in PaperI (thereafter CLUSTER model), suggest the bulge location on the day side (between 7 MLT and 16 MLT) at low geomagnetic activity, opposite to what we have observed in the present study. On the other side, the observed L_{pp} peak on the premidnight side during more active geomagnetic periods is in accordance with CLUSTER results. Our RMSE range of values coincide with those from CLUSTER model. Further comparison with results presented by both *Kwon et al.* [2015] and *Katus et al.* [2015] shows that the plasmapause peak locations derived from our models are consistent with their observations. The first study showed quiet-time plasmapause location derived from medians and means of two years (2008-2009) of THEMIS-based plasmapause crossings, and indicates nearly circular plasmapause with slight bulge in postdusk sector (around 20-22 MLT). This bulge rotates toward dusk under moderate geomagnetic conditions. In the latter study, IMAGE EUV-based plasmapause that results from 43 geomagnetic storms (2000-2002) indicates the bulge position near dusk and across dayside. The MLT of the bulge formation is found to be dependent on the type of solar wind driver. The MLT of the plasmapause peak at low and high geomagnetic activity (characterized with parameter values as listed above) obtained from all above studies are summarized in Table 4.

Finally, we compare the obtained delays in the plasmapause response to the arrival of L_{pp} indicators with those obtained from CLUSTER model in MLT sectors and also when all MLT are taken together (see Table3 in Paper I), and those derived by *Larsen et al.* [2007] from IMAGE EUV plasmapause crossings in 2001 (therefore IMAGE2001 models). Note that IMAGE2001 models provide only the delays of the L_{pp} averaged in MLT. Delay times resulting from our models are generally lower than those obtained based on CLUSTER dataset (see Table3 in Paper I). The delay times derived from all L_{pp} are around 4 hours, significantly lower than the CLUSTER ones which are around 20 hours depending on the indicator. Note however that these delays are close to the values obtained from IMAGE2001 model. For both CRRES2 and CLUSTER models, the time lags increase from postmidnight across dayside to midnight. The correlations between L_{pp} and L_{pp} indicators when all MLTs are taken together are in general similar for these three models, and are between $\sim$ 0.4-0.5.

5. Discussion

In the following we list the obtained results and summarize the comparison with other studies. Our main results are as follows:

i) The quality of developed linear models based on both geomagnetic indices and solar wind coupling functions are very similar, although for solar wind parameters less data were available. The only exception is *Ap* model with somewhat larger RMS errors in all sectors and also when all MLTs are considered.

ii) The quality of developed continuous MLT models are very similar to the quality of the simple linear models. This shows that with adequate data coverage, the simple models can well simulate the plasmapause shape. Only when all local times are considered, the RMSE are reduced compared to that of simpler models.

iii) Simple *GI* models indicate that plasmapause bulge is likely formed between 18 MLT and 00 MLT at quiet times. Solar wind based models cannot resolve whether the bulge is between 18 MLT and 00 MLT or between 00 MLT and 06 MLT. At high geomagnetic activity, all models indicate maximum plasmapause extension on the postdusk/premidnight side.

iv) Developed continuous models place a plasmapause bulge at low geomagnetic activity between 22 MLT and 00 MLT, depending on the model. All these models predict a bulge around 21 MLT for higher geomagnetic activity.

v) The values of the derived delay times of L_{pp} to the arrival of L_{pp} indicators range from 1 to 18 hours, depending on the MLT and on the indicator. For all L_{PP} indicators, the time lag corresponding to the highest correlation is a function of MLT. Lags increase from postmidnight side through dawn to the evening side.

Since different types of L_{pp} indicators (solar wind parameters and geomagnetic indices) provide the same conclusions, we consider our results reliable. As in many previous studies, all of our models show that the plasmapause is closer to the Earth during enhanced geomagnetic activity. The simulated plasmapause shapes are in agreement with past studies for higher level of geomagnetic activity. The differences are found in the comparison with THEMIS1 and CLUSTER models which both indicate the bulge in the day side at low geomagnetic activity. However, important to note is that as geomagnetic activity decreases, the plasmapause becomes more circular and thus, the bulge is less pronounced. Nevertheless, it would be worth to investigate these differences further, e.g., modeling the L_{pp} dataset used to build the THEMIS2 model by including the first harmonic in MLT. This may help to distinguish the influences of the applied method and of the number of used data on the results. When new CLUSTER data will be available, we will perform the analyses to check whether the plasmapause will peak at different MLTs or not at low activity. Generally, the observed discrepancy in the plasmapause shape, as well as in the overall change of the plasmapause radial position likely results from different plasmapause observations, different methodology, unequal number of plasmapause crossings and different parameters used in these studies.

6. Conclusion

In this study we analyse the relationship between different L_{pp} indicators based on both solar wind and geomagnetic indices, and CRRES based plasmapause positions. We built linear fit models for two different data binning (in three and four MLT sectors), and more complex models by including a first harmonic in MLT.

The plasmapause shapes based on all investigated parameters are similar, ensuring that final conclusions are reliable. Monte Carlo bootstrap calculations indicate that Dst provides superior models in the day side. The maximal plasmapause extension is observed in the postdusk side at high geomagnetic activity, confirming findings from previous works. The decrease in the convection electric field places the bulge toward midnight, plasmapause moves away from the Earth and becomes nearly circular. The MLT peak of the plasmapause at low activity should be investigated further, as indicated in the previous section.

The advantage of our approach based on the L_{pp} indicator values at the highest correlation time lags is that it allows to obtain both the MLT plasmapause distribution and the time offset of the plasmapause response to various L_{pp} indicators. With a clear evidence that the time lags corresponding to the highest correlation is a function of MLT, this study verifies the findings presented in Paper I and contributes to constrain the physical mechanism by which the plasmapause is formed. We propose the following simple scenario of the plasmapause formation. Information about L_{PP} indicators during 30 hours before the L_{PP} response reside within the plasmasphere. After 1-4 hours (depending on the indicator), plasmasphere responds in the postmidnight MLT sector, where the formation of the new plasmapause is initiated by the interchange instability. Via mechanism of interchange instability motion proposed by *Lemaire and Pierrard* [2008] and *Pierrard et al.* [2008] the interchange instability propagates to other MLT sectors. In such a way, new plasmapause is formed in all MLTs. The follow-up study dedicated to detailed investigation of the above proposed scenario by employing different dataset is in progress.

The calculated time lags further indicate that after the plasmapause is formed, information is then quickly passed from postmidnight through dawn to noon (likely at higher rate than the co-rotation velocity), and then at somewhat slower rate to midnight. The different time delays obtained from CRRES2, IMAGE2001 and CLUSTER models indicate that the interchange instability by which the plasmapause is formed propagates faster during solar maximum than around solar minimum in the solar activity cycle. This may be associated with the different state of the heliosphere during the studied periods. Namely, both CRESS and IMAGE based L_{pp} cover solar maximum only, while CLUSTER L_{pp} dataset embraces declining phase, minimum, and early ascending phase of the solar cycle. This issue should be investigated further and is left for future study.

Acknowledgments. Geomagnetic indices *Ap*, *Dst* and *AE* are obtained from:
`ftp://ftp.ngdc.noaa.gov/STP/GEOMAGNETIC_DATA/INDICES/KP_AP` and
`http://wdc.kugi.kyoto-u.ac.jp/dstae/index.html`.
The solar wind data are downloaded from OMNIWeb:
`http://omniweb.gsfc.nasa.gov/form/dx1.html`.
The CRRES plasmapause database is available upon request from M. B. Moldwin. V. Pierrard thanks the Scientific Federal Policy for the funding in the framework of the

program Interuniversity Attraction Pole for the project P7/08 CHARM. M.B. Moldwin was partially financed by NSF AGS 1450512.

References

Brice, N. M. (1967), Bulk motion of the magnetosphere, *J. Geophys. Res.*, *72*, 5193–5211.

Carpenter, D. L., and R. R. Anderson (1992), An ISEE/whistler model of equatorial electron density in the magnetosphere, *J. Geophys. Res.*, *97, A2*, 1097–1108.

Cho, J., D.-Y. Lee, J.-H. Kim, D.-K. Shin, K.-C. Kim, and D. Turner (2015), New model fit functions of the plasmapause location determined using THEMIS observations during the ascending phase of Solar Cycle 24, *J. Geophys. Res(Space Physics)*, *120*, 2877–2889, doi:10.1002/2015JA021030.

Darrouzet, F., V. Pierrard, S. Benck, G. Lointier, J. Cabrera, K. Borremans, N. Yu Ganushkina, and J. De Keyser (2013), Links between the plasmapause and the radiation belt boundaries as observed by the instruments CIS, RAPID, and WHISPER onboard Cluster, *J. Geophys. Res.*, *118*, 4176–4188, doi:10.1002/jgra.50239.

Heilig, B., and H. Lühr (2013), New plasmapause model derived from champ field-aligned current signatures, *Ann.Geophys.*, *31(3)*, 529–539, doi:10.5194/angeo-31-529-2013.

Horne, R. B., and R. M. Thorne (1998), Potential waves for relativistic electron scattering and stochastic acceleration during magnetic storms, *Geophys. Res. Lett.*, *25*, 3011–3014, doi:10.1029/98GL01002.

Katus, R. M., D. L. Gallagher, M. W. Liemohn, A. M. Keesee, and L. K. Sarno-Smith (2015), Statistical storm time examination of MLT-dependent plasmapause location derived from IMAGE EUV, *J. Geophys. Res. Space Physics*, *120*, 5545–5559, doi:

10.1002/2015JA021225.

Kozyra, J. U., C. E. Rasmussen, R. H. Miller, and E. Villalon (1995), Interaction of ring current and radiation belt protons with ducted plasmaspheric hiss. 2. Time evolution of the distribution function, *J. Geophys. Res.*, *100*, 21,911–21,920, doi:10.1029/95JA01556.

Kwon, H. J., K. H. Kim, G. Jee, J. S. Park, H. Jin, and Y. Nishimura (2015), Plasmapause location under quiet geomagnetic conditions (Kp less than 1): THEMIS observations, *Geophys. Res. Lett.*, *42*, 7303–7310, doi:10.1002/2015GL066090.

Larsen, B. A., D. M. Klumpar, and C. Gurgiolo (2007), Correlation between plasmapause position and solar wind parameter, *J. Atmosph. Sol. Terr. Phys.*, *69*, 334, doi:10.1016/jastp.2006.06.017.

Lemaire, J., and V. Pierrard (2008), Comparison between two theoretical mechanisms for the formation of the plasmapause and relevant observations, *Geomagnetism and Aeronomy*, *48(5)*, 553–570, doi:10.1134/S0016793208050010.

Lemaire, J. F., and K. I. Gringauz (1998), *The Earth's Plasmasphere*, Cambridge University Press, New York.

Liu, X., and W. Liu (2014), A new plasmapause location model based on themis observations, *Sci China Earth Sci*, *57*, 2552–2557.

Liu, X., W. Liu, J. B. Cao, H. S. Fu, J. Yu, and X. Li (2015), Dynamic plasmapause model based on THEMIS measurements, *J. Geophys. Res. Space Physics*, *120*, 10,543–10,556, doi:10.1002/2015JA021801.

Lorentzen, K. R., J. B. Blake, U. S. Inan, and J. Bortnik (2001), Observations of relativistic electron microbursts in association with VLF chorus, *J. Geophys. Res*, *106*, 6017–6028, doi:10.1029/2000JA003018.

Moldwin, M. B., L. Downward, H. K. Rassoul, R. Amin, and R. R. Anderson (2002), A new model of the location of the plasmapause: CRRES results, *J. Geophys. Res.*, *107(A11)*, 1339, doi:10.1029/2001JA009211.

Newell, P. T., T. Sotirelis, K. Liou, C.-I. Meng, and F. J. Rich (2007), A nearly universal solar wind-magnetosphere coupling function inferred from 10 magnetospheric state variables, *J. Geophys. Res.*, *112,A01216*, doi:10.1029/2006JA012015.

Nishida, A. (1966), Formation of plasmapause, or magnetospheric plasma knee, by the combined action of magnetospheric convection and plasma escape from the tail, *J. Geophys. Res.*, *71*, 5669.

O'Brien, T. P., and M. B. Moldwin (2003), Empirical plasmapause models from magnetic indices, *Geophys. Res. Lett.*, *30(4)*, 1152, doi:10.1029/2002GL016007.

Pierrard, V., and J. Lemaire (2004), Development of shoulders and plumes in the frame of the interchange instability mechanism for plasmapause formation, *Geophys. Res. Lett.*, *31(5),L05809*.

Pierrard, V., G. V. Khazanov, J. Cabrera, and J. Lemaire (2008), Influence of the convection electric field models on predicted plasmapause positions during magnetic storms, *J. Geophys. Res.*, *113,A08212*, doi:10.1029/2007JA012612.

Takahashi, K., and B. J. Anderson (1992), Distribution of ULF energy (f is less than 80 mHz) in the inner magnetosphere - A statistical analysis of AMPTE CCE magnetic field data, *J. Geophys. Res*, *97*, 10,751, doi:10.1029/92JA00328.

Verbanac, G., B. Vršnak, S. Živković, T. Hojsak, A. Veronig, and M. Temmer (2011), Solar wind high-speed streams and related geomagnetic activity in declining phase of solar cycle 23, *Astron. Astrophys.*, *533*, A49–1–A49–6, doi:10.1051/0004-6361/201116615.

Verbanac, G., S. Živković, B. Vršnak, M. Bandić, and T. Hojsak (2013), Comparison of geoeffectiveness of coronal mass ejections and corotating interaction regions, *Astron. Astrophys.*, *558*, A85, doi:10.1051/0004-6361/201220417.

Verbanac, G., V. Pierrard, M. Bandic, F. Darrouzet, J.-L. Rauch, and P. Décréau (2015), Relationship between plasmapause, solar wind and geomagnetic activity between 2007 and 2011, *Ann. Geophys.*, *33*, 1271–1283.

Figure 1. Time lag versus MLT obtained by binning the data into 6-hours MLT for geomagnetic indices (solid lines) and into three MLT sectors for solar wind based L_{PP} indicators (dashed lines).

Figure 2. The L_{pp} in three MLT sectors from linear fit models based on: (left panels) Dst, Ap, AE, and (right panels) V, BV, $d\Phi_{mp}/dt$. Blue and red lines indicate low and high geomagnetic activity as given in Table 5, respectively.

Figure 3. The L_{pp} from: (left panels) linear fit models in four MLT sectors, (right) continuous MLT models. Blue and red lines indicate low and high geomagnetic activity. The symbols indicate the MLT of maximum L_{pp} for each continuous model as given in Table 5, respectively.

Figure 4. Plasmapause shapes obtained from CRRES1 (green), CRRES2 (dark blue), THEMIS1 (light blue), and THEMIS2 (red) models for two levels of geomagnetic activity, low (left panels) and high (right panels). Models based on Dst and AE index are shown at the top and bottom panels, respectively. For details see text.

Table 1. Number of L_{pp} (in three and four sector divisions, and for all MLTs) for investigated L_{pp} indicators. GI represents geomagnetic indices ($GI = Dst, Ap, AE$).

	V	BV	$d\Phi_{mp}/dt$	GI
Sect1 (MLT 01-07)	121	115	115	364
Sect2 (MLT 07-16)	85	84	84	249
Sect3 (MLT 16-01)	94	89	89	350
SectI (MLT 00-06)	129	123	123	393
SectII (MLT 06-12)	78	76	76	226
SectIII (MLT 12-18)	25	24	24	102
SectIV (MLT 18-24)	68	65	65	242
All	300	288	288	963

Table 2. Time–lags Δt (in hours) of the relationship between L_{PP} and L_{PP} indicators (Dst, Ap, AE, V, BV, $d\Phi_{mp}/dt$) for the highest-correlation time–lags obtained with cross–correlation analyses. σs are the RMS errors of the best L_{PP} fits. Subscripts i and all refer to the MLT Sectors 1-3 (01-07 MLT, 07-16 MLT, 16-01 MLT) and to all MLTs sectors, respectively. The last column contains the correlation coefficients (R) obtained when all MLTs are taken together.

	Δt_1	Δt_2	Δt_3	Δt_{all}	σ_1	σ_2	σ_3	σ_{all}	R_{all}
$Dst - L_{pp}$	1	3	10	3	0.75	0.61	0.92	0.83	0.54
$Ap - L_{pp}$	3	8	19	3	0.81	0.72	0.96	0.90	-0.39
$AE - L_{pp}$	1	9	20	4	0.76	0.68	0.92	0.86	-0.49
$V - L_{pp}$	4	3	7	4	0.75	0.61	0.87	0.79	-0.49
$BV - L_{pp}$	4	12	18	4	0.76	0.71	0.90	0.85	-0.40
$d\Phi_{mp}/dt - L_{pp}$	6	9	18	11	0.79	0.73	0.85	0.86	-0.41

Table 3. Time–lags Δt (in hours) of the relationship between L_{PP} and L_{PP} indicators (Dst, Ap, AE) for the highest-correlation time–lags obtained with cross–correlation analyses. The last five columns are the RMS errors (σ) of the best L_{PP} fits. Subscripts i and all refer to the MLT Sectors I-IV (00-06 MLT, 06-12 MLT, 12-18 MLT, 18-00 MLT) respectively.

	Δt_I	Δt_{II}	Δt_{III}	Δt_{IV}	σ_I	σ_{II}	σ_{III}	σ_{IV}
$Dst - L_{pp}$	1	2	7	10	0.74	0.60	0.72	0.97
$Ap - L_{pp}$	3	5	19	28	0.79	0.74	0.73	1.02
$AE - L_{pp}$	1	4	19	29	0.75	0.70	0.67	0.96

Table 4. Linear least-squares fits ($y = ax + b$) for the relationships between L_{PP} and L_{PP} indicators (V, BV, $d\Phi_{mp}/dt$, Dst, Ap, AE) for the highest-correlation time–lags. Subscripts i and all refer to the MLT Sectors 1-3 and to all MLTs sectors, respectively.

	a_1	b_1	a_2	b_2	a_3	b_3	a_{all}	b_{all}
Dst	$(2.00\pm0.15)\times10^{-2}$	4.53 ± 0.05	$(2.03\pm0.15)\times10^{-2}$	4.08 ± 0.06	$(1.53\pm0.16)\times10^{-2}$	4.56 ± 0.06	$(1.93\pm0.10)\times10^{-2}$	4.45 ± 0.03
Ap	$(-2.30\pm0.22)\times10^{-2}$	4.56 ± 0.05	$(-1.45\pm0.18)\times10^{-2}$	3.83 ± 0.06	$(-1.52\pm0.21)\times10^{-2}$	4.49 ± 0.06	$(-1.65\pm0.12)\times10^{-2}$	4.34 ± 0.04
AE	$(-2.48\pm0.19)\times10^{-3}$	4.74 ± 0.06	$(-1.73\pm0.17)\times10^{-3}$	4.06 ± 0.07	$(-1.91\pm0.21)\times10^{-3}$	4.71 ± 0.07	$(-2.04\pm0.12)\times10^{-3}$	4.57 ± 0.04
V	$(-6.80\pm1.11)\times10^{-3}$	7.16 ± 0.48	$(-6.00\pm0.92)\times10^{-3}$	6.41 ± 0.43	$(-4.81\pm1.19)\times10^{-3}$	6.24 ± 0.51	$(-5.75\pm0.65)\times10^{-3}$	6.54 ± 0.29
BV	$(-3.18\pm0.60)\times10^{-1}$	5.27 ± 0.20	$(-2.04\pm0.45)\times10^{-1}$	4.44 ± 0.18	$(-1.66\pm0.66)\times10^{-1}$	4.80 ± 0.26	$(-2.22\pm0.32)\times10^{-1}$	4.87 ± 0.13
$d\Phi_{mp}/dt$	$(-1.39\pm0.28)\times10^{-4}$	4.83 ± 0.13	$(-1.02\pm0.23)\times10^{-4}$	4.11 ± 0.13	$(-1.13\pm0.29)\times10^{-4}$	4.70 ± 0.16	$(-0.92\pm0.13)\times10^{-4}$	4.52 ± 0.08

Table 5. The L_{PP} obtained from the linear least square fits for two values of each of the L_{PP} indicator. The first one is related to the low indicator values, the second one to that at which L_{PP} amounts for $\sim 2.8\ R_E$.

	V ($km\,s^{-1}$)		BV ($mV\,m^{-1}$)		$d\Phi_{mp}/dt$ ($(km\,s^{-1})^{4/3}$ $(nT)^{2/3}$)		Dst (nT)		Ap (nT)		AE (nT)	
	340	580	2	7.5	0.1×10^4	1.35×10^4	10	-60	5	65	30	650
Sect1	4.85	3.22	4.63	2.89	4.69	2.96	4.73	3.33	4.44	3.06	4.66	3.13
Sect2	4.37	2.93	4.03	2.91	4.01	2.74	4.29	2.86	3.76	2.89	4.00	2.93
Sect3	4.61	3.45	4.46	3.55	4.59	3.18	4.72	3.65	4.41	3.50	4.65	3.47
SecAll	4.58	3.20	4.43	3.20	4.42	3.28	4.64	3.29	4.26	3.27	4.51	3.25

Table 6. The parameters of the best fit complex models for the highest-correlation time–lag and RMSE.

	Fit						RMSE				
	$a_1 \times 10^2$	$a_{mlt} \times 10^1$	$(24/2\pi)a_\phi$	b_1	$b_{mlt} \times 10^1$	$(24/2\pi)b_\phi$	σ_1	σ_2	σ_3	σ_4	σ_{all}
Dst	1.91 ± 0.10	2.83 ± 0.77	7.57 ± 1.27	4.42 ± 0.04	0.64 ± 0.13	23.38 ± 0.87	0.75	0.58	0.73	0.95	0.77
Ap	-2.07 ± 0.14	-1.61 ± 0.92	18.85 ± 3.34	4.37 ± 0.04	0.79 ± 0.15	23.16 ± 0.72	0.81	0.71	0.76	1.00	0.83
AE	-0.22 ± 0.01	-1.34 ± 0.72	13.62 ± 2.85	4.57 ± 0.04	0.82 ± 0.14	22.58 ± 0.73	0.76	0.68	0.70	0.95	0.79

Table 7. The MLT of plasmapause peak at low and high geomagnetic activity derived from various models (see text for details). The examined year periods are indicated for each model.

Model	CLUSTER (2007-2011)	CRRES1 (1990-1991)	CRRES2 (1990-1991)	THEMIS1 (2010-2011)	THEMIS2 (2009-2013)	Kwon2015 (THEMIS) (2008-2009)	Katus2015 (IMAGE) (2000-2002)
Low	07-16	22-03	22 - 00	09-12	21	20-21	-
High	16-01	20-22	21	18-20	19	-	around dusk

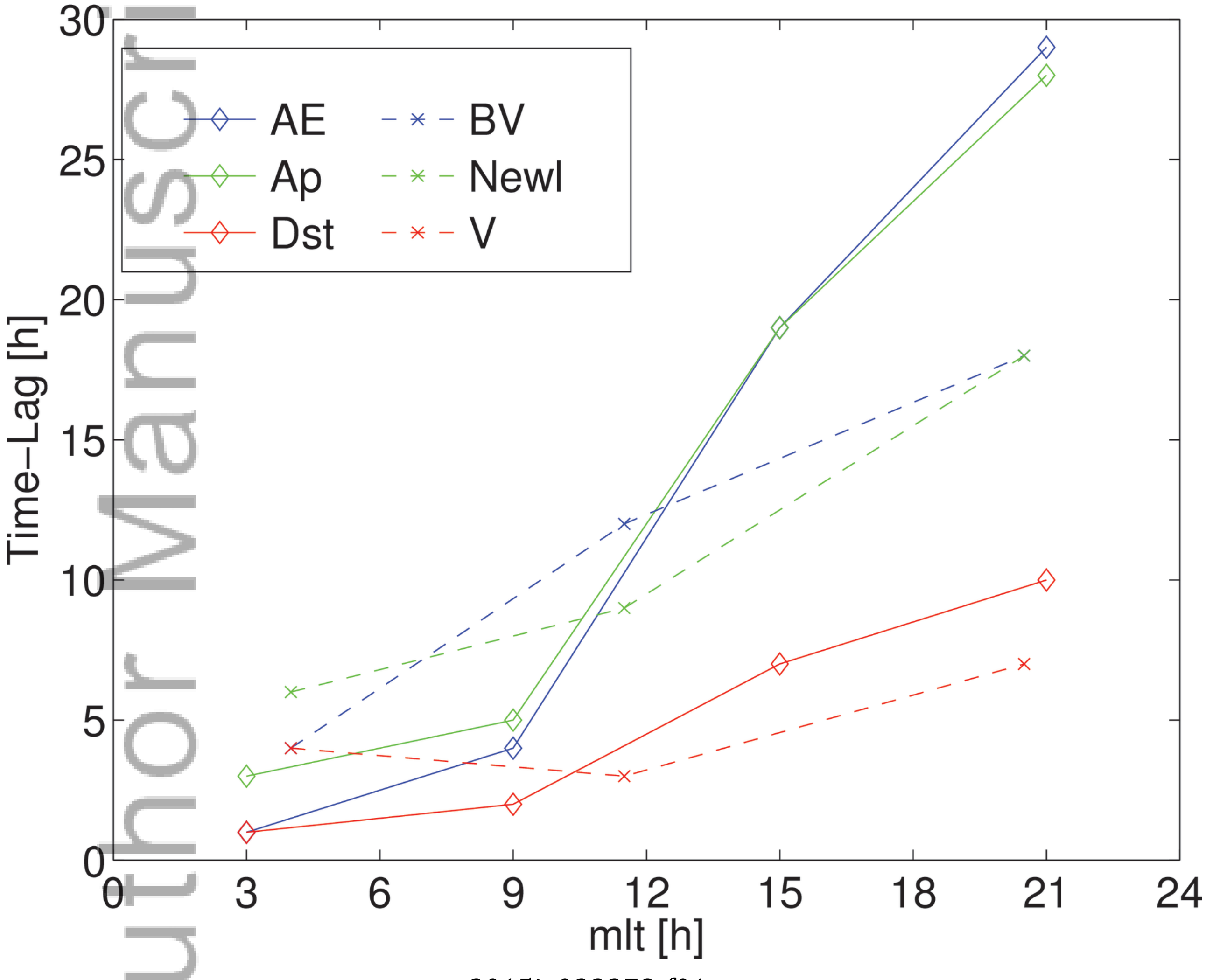

2015ja022278-f01-z-

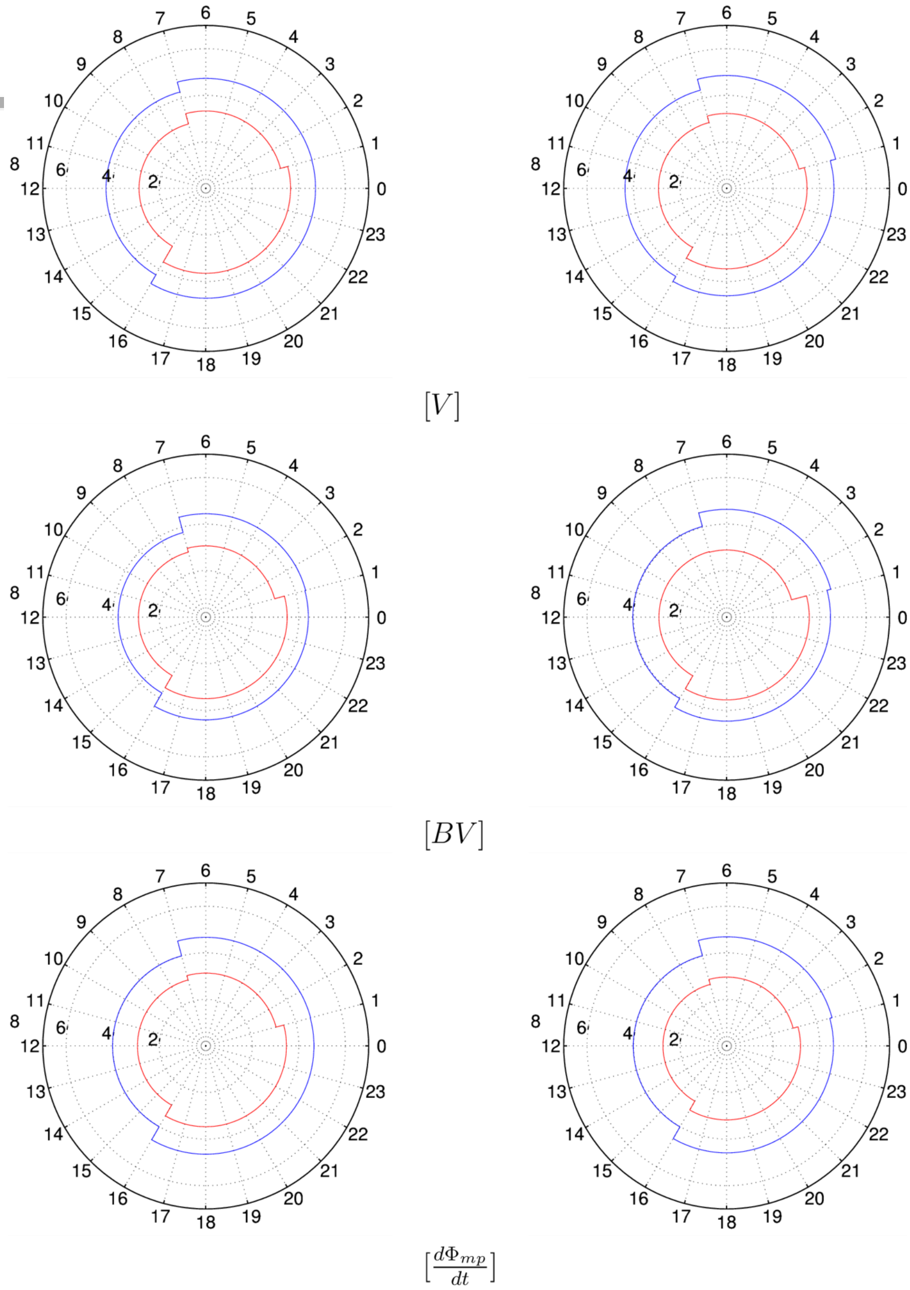

2015ja022278-f02-z-

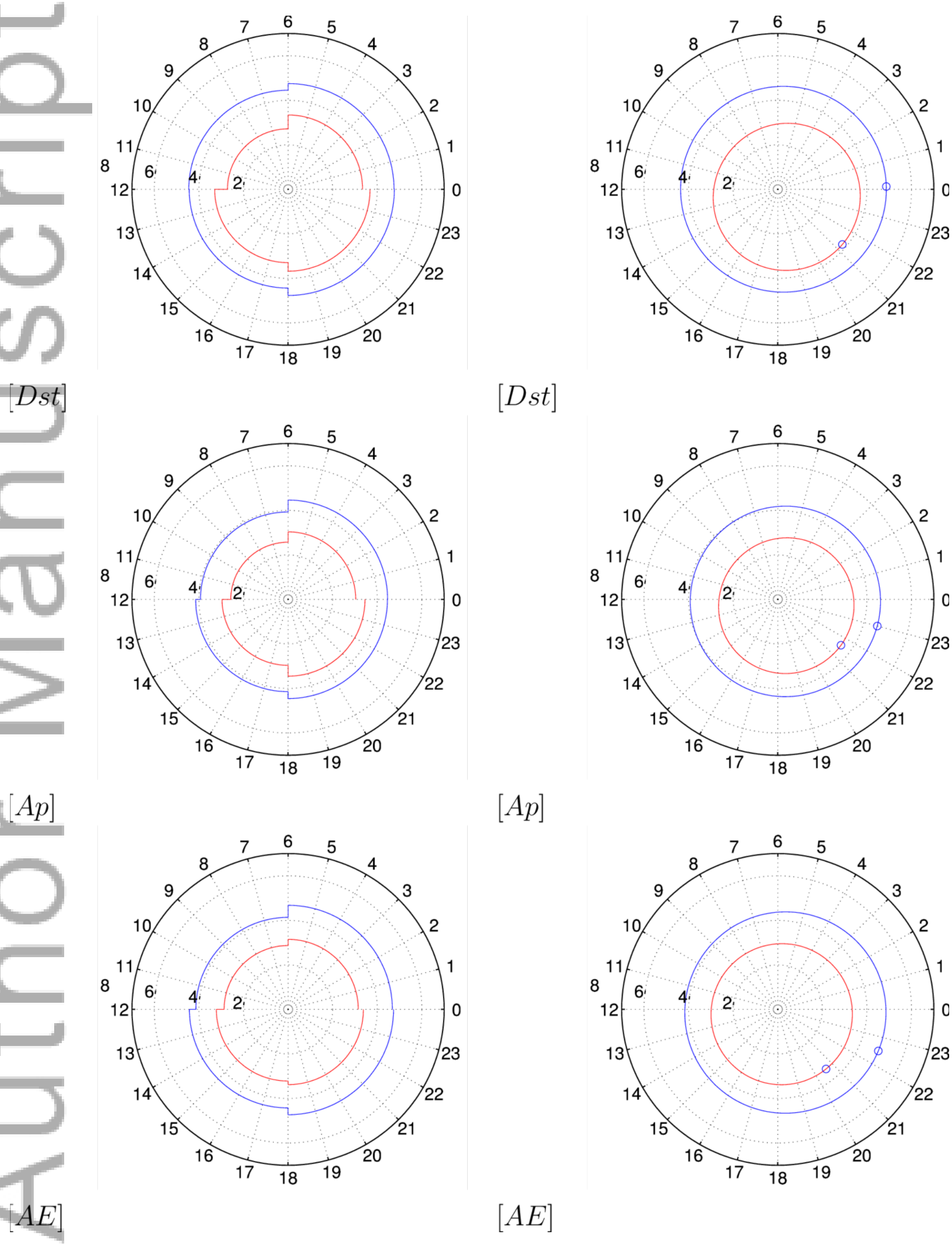

2015ja022278-f03-z-

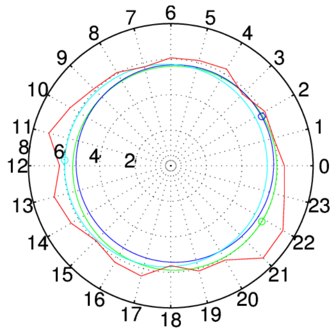

[Dst]

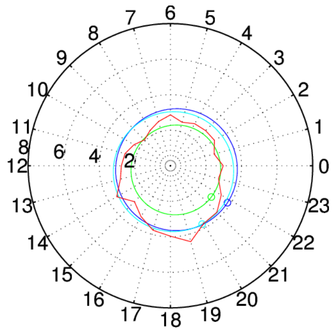

[Dst]

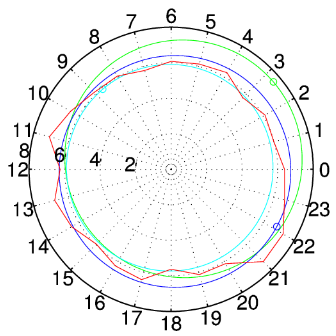

[AE]

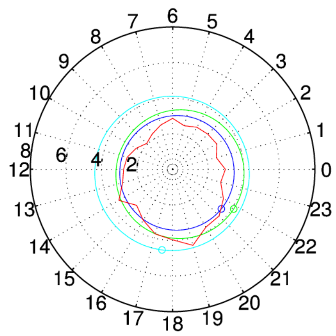

[AE]

2015ja022278-f04-z-